

Ultrafast electron transport in metallic antiferromagnetic Mn₂Au thin films probed by terahertz spectroscopy

Zuanming Jin^{1,2,6,*}, Shunyi Ruan^{2,*}, Xiaofeng Zhou^{3,*}, Bangju Song², Cheng Song^{3,‡}, Xianzhe Chen³, Feng Pan^{1,3}, Yan Peng^{1,6}, Chao Zhang^{1,4}, Guohong Ma^{2,5,§}, Yiming Zhu^{1,6,¶} and Songlin Zhuang^{1,6}

¹Terahertz Technology Innovation Research Institute, Terahertz Spectrum and Imaging Technology Cooperative Innovation Center, Shanghai Key Lab of Modern Optical System, University of Shanghai for Science and Technology, Shanghai 200093, China

²Department of Physics, Shanghai University, Shanghai 200444, China

³Key Laboratory of Advanced Materials, School of Materials Science and Engineering, Tsinghua University, Beijing 100084, China

⁴Institute for Superconducting and Electronic Materials, University of Wollongong, New South Wales 2500, Australia

⁵SIOM & STU Joint Laboratory for superintense lasers and the applications, Shanghai 201210, China

⁶Shanghai Institute of Intelligent Science and Technology, Tongji University, Shanghai 200092, China

 (Received 20 April 2020; revised 1 July 2020; accepted 3 July 2020; published 21 July 2020)

The ultrafast electron transport is central to the requirement of all-electrically controlled spintronics in metallic collinear antiferromagnetic (AFM) Mn₂Au thin films within the terahertz (THz) range. Here we use the THz time-domain spectroscopy to measure the conductivity spectra of Mn₂Au thin films with different thicknesses and temperatures. We demonstrate an onset of carrier localization in Mn₂Au with decreasing the film thickness from 15 to 5 nm. By using optical pump-THz probe spectroscopy, we found the surface trapping states in the thinnest Mn₂Au film limit its photoconductivity significantly. The DC conductivity and scattering time become larger and longer with decreasing temperature for all samples, which suggests that Mn₂Au behaves in a typical metallic fashion. The THz optical and conductivity properties of Mn₂Au films will advance our understanding of ultrafast electronic transport processes in AFM Mn₂Au thin films.

DOI: [10.1103/PhysRevB.102.014438](https://doi.org/10.1103/PhysRevB.102.014438)

I. INTRODUCTION

With the rapid development of spintronics, increasing interest has been attached to the metallic antiferromagnet [1,2]. Mn₂Au was theoretically proposed to be a robust antiferromagnet with a high Néel temperature above 1000 K [3]. Mn₂Au has been experimentally demonstrated to be a good electrical conductor and an antiferromagnet with broken sublattice inversion symmetry [4]. The magnetic moments of metallic Mn₂Au can be manipulated by Néel spin-orbit torque (NSOT) [5]. Efficient electrical switching is at the center of its application in high-density and ultrafast nonvolatile memories [6]. Bringing the switching of Néel spin vector by pulsed DC currents towards the THz frequency range is the key advance for realization of ultrafast switching in Mn₂Au thin film [7].

Because the charge current produced NSOT depends on the conductivity of metallic Mn₂Au film, the ultrafast electronic transport properties are crucial for switching the sublattice magnetization by using THz pulses. Therefore, in spite of all its promise, the electron transport and photoinduced conductivity dynamics in Mn₂Au thin film still remains to be shown. We outline here the key challenge for the electronic properties

of metallic AFM alloys. First of all, the quantitative extraction of the complex conductivity of a nanometer-thick sample in a contact-free fashion. Second, the thickness- and temperature-dependent electron transport parameters are required. We overcome these challenges by a combination of two different THz spectroscopies, fully satisfying the above requirements to directly access the ultrafast electronic properties of magnetic order materials without fabrication micro/nanometer-scale devices with electrodes [8–11].

In this paper we experimentally study the thickness- and temperature-dependent sheet conductivity spectra of Mn₂Au films by THz time-domain spectroscopy (THz-TDS), which are well described by the Drude-Smith model and then yield the DC conductivity, carrier momentum scattering time, and carrier localization parameter. We find the DC conductivity and scattering time become larger and longer with decreasing temperature, respectively. Furthermore, the carrier momentum scattering time decreases monotonously with decreasing the thickness. By using optical pump-THz probe spectroscopy (OPTP), we also determine the time-resolved photoconductivity response of different thickness samples upon photoexcitation.

II. SAMPLES AND METHODS

The 5-, 10-, and 15-nm-thick (103) oriented Mn₂Au films were deposited on 500 μm single-crystal (100) MgO substrates with the size of 5 × 5 mm² by magnetron sputtering at 300 °C [12]. The base pressure is 2.5 × 10⁻⁵ Pa, and

*These authors contributed equally to this work.

†Corresponding author: physics_jzm@usst.edu.cn

‡songcheng@mail.tsinghua.edu.cn

§ghma@staff.shu.edu.cn

¶ymzhu@usst.edu.cn

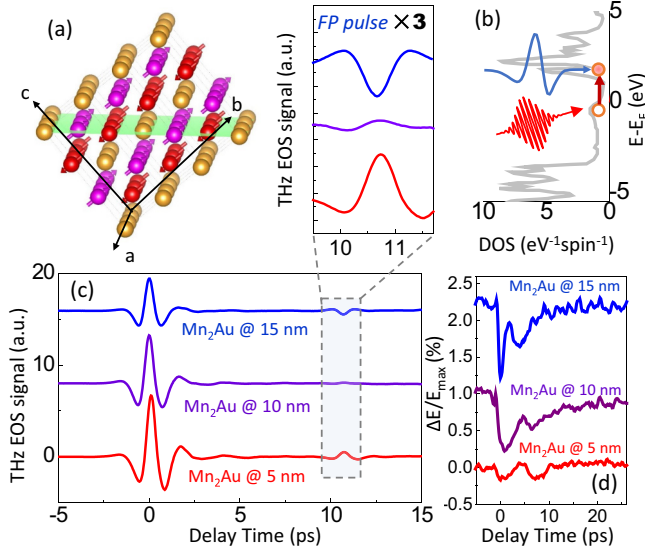


FIG. 1. (a) Schematic unit cells of Mn₂Au. The magnetic moments of the neighboring sublattices are opposing. (b) Schematic photoexcitation of electrons above the Fermi surface with the DOS of Mn₂Au film [14]. (c) Transmitted THz pulses through the 5-, 10-, and 15-nm-thick samples. The inset zooms in the internal reflections inside the dashed box. (d) By varying the delay time between pump and probe pulses to measure the THz peak field modulation of three Mn₂Au thin films at room temperature. All the traces are vertically shifted for clarity.

the growth rate is 0.07 nm/s using a Mn₂Au alloy target (atomic ratio of 2:1) [13]. Further details of sample treatment, structural and magnetic properties, can be found in Refs. [12,13]. Figure 1(a) shows a schematic of unit cells of Mn₂Au, where the (103) plane of Mn₂Au is highlighted. Figure 1(b) illustrates the density of state (DOS) of Mn₂Au, which is dominated by the Mn atom contributions. DOS of Mn₂Au has mainly a character of a 3d band in the energy range from -4 to +4 eV [6,14].

A standard THz-TDS was driven by a mode-locked, centered wavelength at a 800 nm Ti:sapphire oscillator [15]. The output beam was split into two laser beams, one was used to generate the THz wave and the other was applied to detect the THz transient. The THz wave produced by the photoconductive antenna focused on the sample by a polyethylene lens. And then, the THz wave was collected by a detector antenna. Moving the optical delay, we can map out the time-resolved THz signals. Our OPTP measurement was driven by a Ti:sapphire amplifier operating at a repetition rate of 1 kHz, generating 120 fs pulses at a central wavelength of 800 nm [16]. The linearly polarized pump laser pulse was normally incident on the sample. THz radiation was detected by free space electro-optical sampling with a 1.0-mm-thick (110) ZnTe crystal using the standard lock-in technique. The spot sizes of the optical pump and the THz probe at the sample were 5.0 and 2.5 mm, respectively. A THz-transparent laser beam block was placed behind the sample to stop the propagation of the remainder of the pump laser beam. The OPTP measurements were performed at room temperature. In the one-dimensional (1D) operation of OPTP, we fix the

THz waveform at the THz peak, and then scan the delay line to measure the transmitted THz electric-optical sampling (EOS) signal and the photoinduced change as a function of pump-probe time delay. For this mode, we do not map out the entire THz waveform, and therefore do not obtain any frequency-resolved information (see Supplemental Material 1 for the experimental methods in detail) [17].

III. EXPERIMENTAL RESULTS AND DISCUSSION

Figure 1(c) shows the measured time-domain THz EOS signals transmitted through three Mn₂Au films with the thickness of 5, 10, and 15 nm on MgO substrates. After the primary THz pulse, we observe a small THz pulse induced by Fabry-Perot (FP) reflections inside the MgO substrate. The ~11 ps delay of the FP reflection agrees with one roundtrip (twice the optical path) through the MgO substrate of 0.5 mm thickness with a refractive index of about 3.4. The change in polarity of the FP reflection will be discussed later. One can see that the amplitude of the primary THz pulse decreases with increasing the Mn₂Au thickness. Figure 1(d) shows the photoinduced modulation in the transmitted THz peak field ΔE(Δt)/E_{max} as a function of pump-probe delay time (Δt), where E_{max} is the peak value of the transmitted THz EOS signal without optical excitation. Δt = 0 is defined as the temporal overlap of the fs excitation pulse with the peak field strength of the THz probe pulse. The negative rapid drop in the ΔE(Δt)/E_{max} indicates an increase of THz absorption, caused by the photoinduced free-carriers.

Since the metallic Mn₂Au is largely dominated by the conductive response, we analyzed the spectral data in terms of the complex conductivity. The complex conductivity can be derived from the THz EOS pulses transmitted through the MgO substrate E_{MgO}(ω), and through the Mn₂Au on the MgO substrate E_{MgO+Mn₂Au}(ω). As the thicknesses of conducting films are much smaller than the wavelength and the skin depth, the thin conduction film approximation (Tinkham formula) can be used to extract the complex conductivity [11],

$$\frac{E_{\text{MgO}+\text{Mn}_2\text{Au}}(\omega)}{E_{\text{MgO}}(\omega)} = \frac{1 + n_{\text{MgO}}}{1 + n_{\text{MgO}} + Z_0\sigma(\omega)d} e^{i\frac{\omega}{c}(n-1)\Delta L}, \quad (1)$$

where $Z_0 = \sqrt{\mu_0/\epsilon_0} = 377 \Omega$ is the impedance of free space, d is the thickness of Mn₂Au film, and the sheet conductivity $\sigma_{\text{sheet}}(\omega) = \sigma(\omega)d$. The mean refractive index of the MgO $n_{\text{MgO}} \approx 3.4$ is measured within 0.4–1.6 THz (see Supplemental Material 2) [17], which is consistent with the value reported in Ref. [18]. Noted that the thickness difference ΔL between sample and reference MgO substrate is 1.92 μm (5 nm sample), ΔL = 2.02 μm (10 nm sample) and ΔL = 2.45 μm (15 nm sample), which are obtained by the THz echo calibration (see the details in Supplemental Material 2) [17]. It is therefore necessary to consider the influences of thickness difference on the real (σ₁) and imaginary (σ₂) parts of the sheet conductivities σ_{sheet}(ω) for 5-, 10-, and 15-nm-thick samples at 300 K. Furthermore, the photoinduced frequency-integrated sheet conductivity dynamics can be derived from the ΔE(Δt)/E_{max} data [19,20],

$$\Delta\sigma_{\text{sheet}}(\Delta t) = \frac{1 + n_{\text{MgO}}}{Z_0} \left(\frac{1}{1 + \Delta E(\Delta t)/E_{\text{max}}} - 1 \right). \quad (2)$$

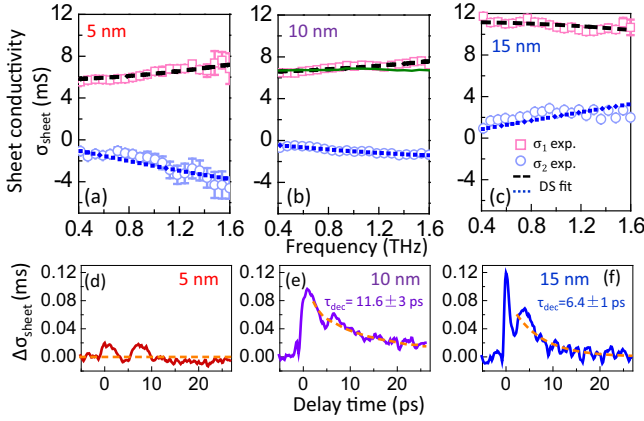


FIG. 2. (a)–(c) The real and imaginary parts of the complex conductivity spectra and (d)–(f) photoinduced sheet conductivity dynamics of 5-, 10-, and 15-nm-thick Mn₂Au films at 300 K. The dashed and dotted lines present the best fits with the DS model. The green curve in (b) is a theoretical curve of the impedance matching for the best antireflection performance. Error bars inside the symbols denote the standard errors. The orange lines in (e) and (f) are the single exponential decay fittings.

Figures 2(a)–2(c) show the real $\sigma_1(\omega/2\pi)$ and the imaginary $\sigma_2(\omega/2\pi)$ components of the complex sheet conductivity measured for 5-, 10-, and 15-nm-thick samples at 300 K. $\sigma_1(\omega/2\pi)$ represents the current response, which is in-phase with the THz driving field. While $\sigma_2(\omega/2\pi)$ represents the $\pi/2$ out-of-phase inductive current. For the 15 nm Mn₂Au film [Fig. 2(c)], both $\sigma_1(\omega/2\pi)$ and $\sigma_2(\omega/2\pi)$ are positive, showing a good metallic state. With decreasing the thickness, $\sigma_2(\omega/2\pi)$ becomes negative and shows a decreasing function of THz frequency, indicating a poor conductive behavior [21], as shown for 5 and 10 nm films in Figs. 2(a) and 2(b). Figures 2(d)–2(f) show the photoinduced frequency-integrated sheet conductivity $\Delta\sigma_{\text{sheet}}(\Delta t)$ for three samples with an excitation fluence of ~ 2.04 mJ/cm². $\Delta\sigma_{\text{sheet}}(\Delta t)$ are positive for all Mn₂Au samples. It derives from the increasing of carrier concentration caused by the interband transition [Fig. 1(b)]. Clearly, in the present case, the 15 nm sample shows the largest peak value of $\Delta\sigma_{\text{sheet}}(\Delta t)$ among three Mn₂Au samples. A single exponential function was used to estimate the decay time constant $\tau_{\text{dec}} = 6.4 \pm 1$ and 11.6 ± 3 ps for the 15 and 10 nm films, respectively. While for the 5 nm sample, the maximum value of $\Delta\sigma_{\text{sheet}}(\Delta t)$ is around 5 times smaller than that observed for the thicker samples, which may be due to free-charge recombination or trapping at surface defect states [22].

We present the complex conductivities measured at different temperatures, as shown in Figs. 3(a)–3(d), 3(e)–3(h), and 3(i)–3(l) of 5-, 10-, and 15-nm-thick Mn₂Au films, respectively. We cannot identify any phonons and magnons throughout the probed frequency range. It can be seen that $\sigma_1(\omega/2\pi)$ and $\sigma_2(\omega/2\pi)$ become more significantly frequency dependent, with decreasing temperature. To describe the dependence of the complex conductivity function on the material parameters related to the transport of free charge, the widely used approach is the Drude-Smith (DS)

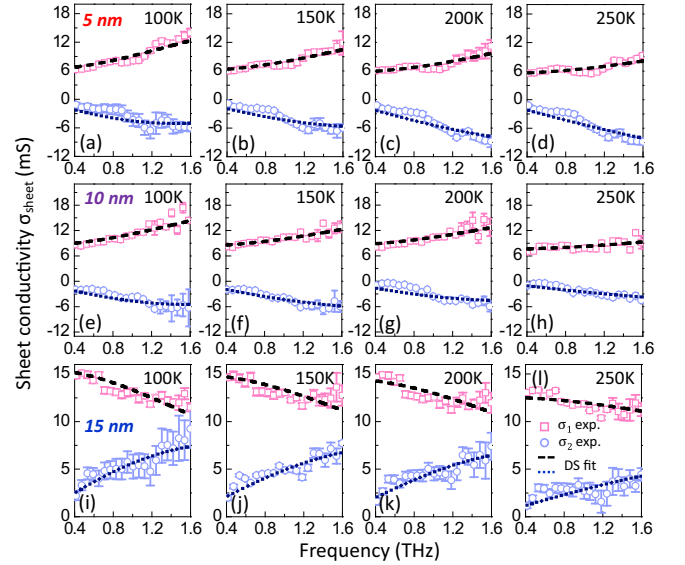


FIG. 3. The real and imaginary parts of the conductivity spectra of the (a)–(d) 5-, (e)–(h) 10-, and (i)–(l) 15-nm-thick Mn₂Au thin films at 100, 150, 200, and 250 K. The DS model fits are also plotted in the figures.

model [23]

$$\tilde{\sigma}_{\text{sheet}}(\omega) = \frac{\sigma_{\text{sheet, DC}}}{1 - i\omega\tau} \left[1 + \frac{c}{1 - i\omega\tau} \right], \quad (3)$$

where $\sigma_{\text{sheet, DC}}$ is the sheet DC conductivity, τ is the momentum scattering time. DS model is based on the dispersive free charge transport in a disordered medium. The carriers retain part of their initial velocity upon scattering. $c = -1$ and 0 representing the carrier's momentum is completely backscattered and randomized, respectively [24]. Figures 2(a)–2(c) and Fig. 3 show that the experimental results can be fitted very well using the DS model. We use the R-square to evaluate the DS fitting in Supplemental Material 3 [17]. It is evident that the measured material response is to the largest extent DS dominated. The parameters of electron transport $\sigma_{\text{sheet, DC}}$, τ , and c as functions of the thickness and temperature are summarized in Fig. 4.

Figure 4(a) shows that $\sigma_{\text{sheet, DC}} = \frac{Ne^2}{m^*} \tau(1 + c)d$ is nearly proportional to the sample thickness. In Fig. 4(b) it can be found that $\sigma_{\text{sheet, DC}}$ have slight increases with decreasing temperature. This finding is consistent with the temperature-dependent resistivity of a Mn₂Au layer reported by Jourdan *et al.*, which decreases with decreasing temperature [25]. Furthermore, using the $\sigma_{\text{sheet, DC}}$ extracted by the DS model as shown in Fig. 4(a), we calculate the $\Delta n = n_{\text{MgO}} - n_{\text{air}} - Z_0\sigma_{\text{sheet, DC}}$ for three different-thickness samples [26]. The $n_{\text{MgO}} = 3.4$, $n_{\text{air}} = 1$, and $Z_0 = 377\Omega$ are assumed to be constants within the THz frequency range. For the 5 nm sample, $\Delta n = 0.44 > 0$. Compared to the incident primary THz pulse, it corresponds to a zero-phase shift of the FP pulse. For the 15 nm sample, $\Delta n = -1.82 < 0$ corresponds to a π -phase shift of the FP pulse. While for the 10 nm sample, $\Delta n = -0.06$ is approaching zero (impedance matching condition) [27], therefore the FP pulse is significant suppressed, as shown

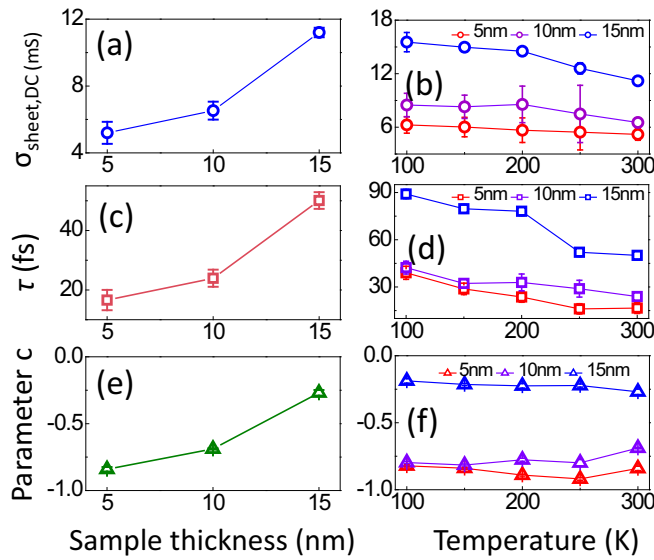


FIG. 4. The fit parameters $\sigma_{\text{sheet, DC}}$, τ , and c are plotted in (a), (c), and (e), respectively, for various film thickness at room temperature. (b), (d), and (f) The temperature-dependent $\sigma_{\text{sheet, DC}}$, τ , and c , respectively, for the 5-, 10-, and 15-nm-thick samples.

in the inset of Fig. 1(c). In order to perfectly eliminate all back reflections at the interface through impedance matching, we calculate the real part of sheet conductivity $\sigma_1(\omega/2\pi) = \frac{n_{\text{MgO}} - n_{\text{air}}}{Z_0}$, as the green curve shown in Fig. 2(b). It can be found that the conductance of 10-nm-thick Mn_2Au film roughly matches the THz impedance between the MgO substrate and the surrounding air, thus acting as a very broadband antireflection coating (see Supplemental Material 4) [17].

As shown in Fig. 4(c), τ decreases monotonously with decreasing the thickness. $\tau = 50.1 \pm 2.8$, 23.9 ± 2.8 , and 16.6 ± 3.4 fs for 15, 10, and 5 nm samples, respectively. The values are very similar to the values obtained from both ferromagnetic iron thin films [28] and antiferromagnet Mn_3Sn thin films [29]. In addition, Fig. 4(e) shows that $c = -0.26 \pm 0.02$ @ 15 nm film decreases to -0.84 ± 0.01 @ 5 nm film. As the probability of an electron scattering on the surface depends on its mean free path in the bulk [30]. When the film becomes thicker, the effect of surface scattering become less obvious, thus the free carriers are conducting with a longer mean free path in the bulk material. With decreasing the thickness, our observations indicate that the charge carriers are scattered

more often, which suggests an onset of carrier back scattering or localization caused by disorder in the surface structure.

The crossover between $c = 0$ and -1 in the Mn_2Au thin films can also be interpreted as a transition from an inductive response ($c > -0.5$, $\sigma_2 > 0$) of electrons to the external electric field to a capacitive response ($c < -0.5$, $\sigma_2 < 0$) [24]. In Fig. 4(d), τ become longer with decreasing temperature for all three samples, which behaves in a typical metallic fashion. Furthermore, Fig. 4(f) shows the mean values of $c = -0.22 \pm 0.03$, -0.77 ± 0.05 , and -0.86 ± 0.04 for 15, 10, and 5 nm films, respectively, within the temperature range from 100 to 300 K.

IV. CONCLUSIONS

In summary, we have combined THz-TDS and OPTP to investigate the THz conductivity of the metallic AFM Mn_2Au thin films. With decreasing the thickness from 15 to 5 nm, we report an onset of carrier localization in Mn_2Au thin film. We find that the surface trapping states limit the photoinduced conductivity dynamics in the 5 nm Mn_2Au film. Temperature-dependent THz conductivities do not exhibit any phonons and magnons within the current THz frequency region. The DC conductivity and scattering time become larger and longer with decreasing temperature, as are usual in metals. The crossover between $c = -0.22 \pm 0.03$ @ 15 nm film and -0.86 ± 0.04 @ 5 nm Mn_2Au thin film indicates a transition from an inductive response of electrons to the external electric field to a capacitive response. The ultrafast electronic transports and THz optical properties of Mn_2Au films provide groundwork for the ultimate technological applications of this important metallic antiferromagnet.

ACKNOWLEDGMENTS

This work is supported by the National Natural Science Foundation of China (Grants No. 61975110, No. 11604202, No. 11674213, No. 61735010, No. 51871130, and No. 61722111); the 111 Project (Grant No. D18014); the International Joint Lab Program supported by Science and Technology Commission Shanghai Municipality (Grant No. 17590750300); The Key project supported by Science and Technology Commission Shanghai Municipality (Grant No. YDZX20193100004960). Science and Technology Commission of Shanghai Municipality (Shanghai Rising-Star Program Grant No. 18QA1401700). Shanghai Educational Development Foundation (Grant No. 16CG45). Young Chang Jiang Scholars Program and Beijing Innovation Center for Future Chip (ICFC).

[1] V. Baltz, A. Manchon, M. Tsoi, T. Moriyama, T. Ono, and Y. Tserkovnyak, Antiferromagnetic spintronics, *Rev. Mod. Phys.* **90**, 015005 (2018).
 [2] T. Jungwirth, X. Marti, P. Wadley, and J. Wunderlich, Antiferromagnetic spintronics, *Nat. Nanotechnol.* **11**, 231 (2016).
 [3] S. Khmelevskiy and P. Mohn, Layered antiferromagnetism with high Néel temperature in the intermetallic compound Mn_2Au , *Appl. Phys. Lett.* **93**, 162503 (2008).

[4] H. Wu, Z. Liao, R. G. S. Sofin, G. Feng, X. Ma, A. B. Shick, O. N. Mryasov, and I. V. Shvets, Mn_2Au : Body-centered-tetragonal bimetallic antiferromagnets grown by molecular beam epitaxy, *Adv. Mater.* **24**, 6374 (2012).
 [5] J. Železný, H. Gao, K. Výborný, J. Zemen, J. Mašek, A. Manchon, J. Wunderlich, J. Sinova, and T. Jungwirth, Relativistic Néel-Order Fields Induced by Electrical Current in Antiferromagnets, *Phys. Rev. Lett.* **113**, 157201 (2014).

- [6] S. Y. Bodnar, L. Šmejkal, I. Turek, T. Jungwirth, O. Gomonay, J. Sinova, A. A. Sapozhnik, H. -J. Elmers, M. Kläui, and M. Jourdan, Writing and reading antiferromagnetic Mn_2Au by Néel spin-orbit torques and large anisotropic magnetoresistance, *Nat. Commun.* **9**, 348 (2018).
- [7] K. Olejník, T. Seifert, Z. Kašpar, V. Novák, P. Wadley, R. P. Champion, M. Baumgartner, P. Gambardella, P. Němec, J. Wunderlich, J. Sinova, P. Kužel, M. Müller, T. Kampfrath, and T. Jungwirth, Terahertz electrical writing speed in an antiferromagnetic memory, *Sci. Adv.* **4**, eaar3566 (2018).
- [8] Z. Jin, A. Tkach, F. Casper, V. Spetter, H. Grimm, A. Thomas, T. Kampfrath, M. Bonn, M. Kläui, and D. Turchinovich, Accessing the fundamentals of magnetotransport in metals with terahertz probes, *Nat. Phys.* **11**, 761 (2015).
- [9] A. D. Jameson, J. W. Kevek, J. L. Tomaino, M. Hemphill-Johnston, M. J. Paul, M. Koretsky, E. D. Minot, and Y. Lee, Terahertz spectroscopy of Ni–Ti alloy thin films, *Appl. Phys. Lett.* **98**, 221111 (2011).
- [10] K. L. Krewer, Z. Mics, J. Arabski, G. Schmerber, E. Beaupaire, M. Bonn, and D. Turchinovich, Accurate terahertz spectroscopy of supported thin films by precise substrate thickness correction, *Opt. Lett.* **43**, 447 (2018).
- [11] B. Cheng, Y. Wang, D. Barbalas, T. Higo, S. Nakatsuji, and N. P. Armitage, Terahertz conductivity of the magnetic Weyl semimetal Mn_3Sn films, *Appl. Phys. Lett.* **115**, 012405 (2019).
- [12] X. F. Zhou, J. Zhang, F. Li, X. Z. Chen, G. Y. Shi, Y. Z. Tan, Y. D. Gu, M. S. Saleem, H. Q. Wu, F. Pan, and C. Song, Strong orientation-dependent spin-orbit torque in thin films of the antiferromagnet Mn_2Au , *Phys. Rev. Appl.* **9**, 054028 (2018).
- [13] X. F. Zhou, X. Z. Chen, J. Zhang, F. Li, G. Y. Shi, Y. M. Sun, M. S. Saleem, Y. F. You, F. Pan, and C. Song, From fieldlike torque to antidamping torque in antiferromagnetic Mn_2Au , *Phys. Rev. Appl.* **11**, 054030 (2019).
- [14] X. Chen, X. Zhou, R. Cheng, C. Song, J. Zhang, Y. Wu, Y. Ba, H. Li, Y. Sun, Y. You, Y. Zhao, and F. Pan, Electric field control of Néel spin–orbit torque in an antiferromagnet, *Nat. Mater.* **18**, 931 (2019).
- [15] J. Li, S. Yang, X. Chen, N. Zhuang, Q. Zhu, A. Wu, X. Lin, G. Ma, Z. Jin, and J. Yao, Temperature-dependent dielectric characterization of magneto-optical $\text{Tb}_3\text{Sc}_2\text{Al}_3\text{O}_{12}$ crystal investigated by terahertz time-domain spectroscopy, *Chin. Phys. Lett.* **36**, 044203 (2019).
- [16] X. Xing, L. Zhao, Z. Zhang, L. Fang, Z. Fan, X. Liu, X. Lin, J. Xu, J. Chen, X. Zhao, Z. Jin, and G. Ma, Photoinduced terahertz conductivity and carrier relaxation in thermal-reduced multilayer graphene oxide films, *J. Phys. Chem. C* **121**, 2451 (2017).
- [17] See Supplemental Material at <http://link.aps.org/supplemental/10.1103/PhysRevB.102.014438> for details on experimental methods, accurate THz conductivity spectrum by precise substrate thickness correction, the impedance matching condition, and the x-ray diffraction (XRD) spectrum of the sample.
- [18] Y. Hu, C. Zhang, J. Shen, and X. C. Zhang, Time-domain terahertz spectroscopy of (100) MgO and (100) LaAlO_3 substrates *Acta Phys. Sin.* **53**, 1772 (2004).
- [19] P. Parkinson, J. Lloyd-Hughes, M. B. Johnston, and L. M. Herz, Efficient generation of charges via below-gap photoexcitation of polymer-fullerene blend films investigated by terahertz spectroscopy, *Phys. Rev. B* **78**, 115321 (2008).
- [20] J. Kim, K. Jeong, M. Baik, D. Kim, J. Chae, H. Park, S. Hong, D. Ko, and M. Cho, Quantification of point and line defects in $\text{Si}_{0.6}\text{Ge}_{0.4}$ alloys with thickness variation via optical pump-THz probe measurement, *Appl. Surf. Sci.* **513**, 145815 (2020).
- [21] M. Walther, D. G. Cooke, C. Sherstan, M. Hajar, M. R. Freeman, and F. A. Hegmann, Terahertz conductivity of thin gold films at the metal-insulator percolation transition, *Phys. Rev. B* **76**, 125408 (2007).
- [22] H. Liu, J. Lu, H. F. Teoh, D. Li, Y. P. Feng, S. H. Tang, C. H. Sow, and X. Zhang, Defect Engineering in $\text{CdS}_x\text{Se}_{1-x}$ nanobelts: An insight into carrier relaxation dynamics via optical pump–terahertz probe spectroscopy, *J. Phys. Chem. C* **116**, 26036 (2012).
- [23] N. V. Smith, Classical generalization of the Drude formula for the optical conductivity, *Phys. Rev. B* **64**, 155106 (2001).
- [24] A. Thoman, A. Kern, H. Helm, and M. Walther, Nanostructured gold films as broadband terahertz antireflection coatings, *Phys. Rev. B* **77**, 195405 (2008).
- [25] M. Jourdan, H. Bräuning, A. Sapozhnik, H. -J. Elmers, H. Zabel, and M. Kläui, Epitaxial Mn_2Au thin films for antiferromagnetic spintronics, *J. Phys. D: Appl. Phys.* **48**, 385001 (2015).
- [26] K. Neeraj, S. Choudhury, D. Polley, R. Acharya, J. Sinha, A. Barman, and R. K. Mitra, Efficient terahertz anti-reflection properties of metallic anti-dot structures, *Opt. Lett.* **42**, 1764 (2017).
- [27] J. Kröll, J. Darmo, and K. Unterrainer, Metallic wave-impedance matching layers for broadband terahertz optical systems, *Opt. Express* **15**, 6552 (2007).
- [28] K. L. Krewer, W. Zhang, J. Arabski, G. Schmerber, E. Beaupaire, M. Bonn, and D. Turchinovich, Thickness-dependent electron momentum relaxation times in iron films, *Appl. Phys. Lett.* **116**, 102406 (2020).
- [29] T. Matsuda, N. Kanda, T. Higo, N.P. Armitage, S. Nakatsuji, and R. Matsunaga, Room-temperature terahertz anomalous Hall effect in Weyl antiferromagnet Mn_3Sn thin films, *Nat. Commun.* **11**, 909 (2020).
- [30] E. H. Sondheimer, The mean free path of electrons in metals, *Adv. Phys.* **1**, 1 (1952).